Particuology 57 (2021) 82–94

Contents lists available at ScienceDirect

Particuology

journal homepage: www.elsevier.com/locate/partic

Particulate aggregation through a modulated annular one-dimensional acoustic field at resonant frequencies

Zhenghui Qiao[a,b,*], Xiaojun Pan[a], Shaohua Liang[a], Xiaolong Bi[a], Juan Wang[a], Wei Xie[a], Kang Wang[a], Yanwen Wang[a], Jun Fang[a], Xuefei Zhu[a], Shaoxin Sun[a], Shaohui Li[b]

[a] College of Energy and Power Engineering, Nanjing Institute of Technology, Nanjing 211167, China
[b] Key Laboratory of Energy Thermal Conversion and Control of Ministry of Education, School of Energy and Environment, Southeast University, Nanjing 210096, China

ARTICLE INFO

Article history:
Received 6 August 2020
Received in revised form
14 November 2020
Accepted 22 November 2020

Keywords:
Acoustic aggregation
Porous particulates
Secondary radiation force
Acoustic radiation force
Stripe pattern
Inhomogeneous field

ABSTRACT

The visualization and analysis of a novel acoustic-particulate system is the objective of this study. The system is composed of rice-husk fired smoke particulates (36.7 nm–840 μm) and one annular resonant circular-tube waveguide contrarily coupled with two sound sources. The collective interaction behavior process of smoke particulates in an inhomogeneous acoustic field is displayed during an experiment and a simulation. The result shows that the aggregation and fragmentation of particles under a change in resonant frequencies and sound pressure amplitude is extremely complex. This complex process consists of dynamically tuning the particle characteristics to attain stripes shaped like thin-films/umbrellas and clusters with volume-change/fragmentation. The balanced modulation of the acoustic radiation force and secondary radiation force to alter the particle characteristics (size and stack density) is verified to be the control mechanism of the particle system. The intermediate variable of the process control is the acoustic contrast factor (Φ) related to the physical characteristics of the growing particulates. The value plus-minus alternation of Φ results in different particulate processes. This study can enhance the application of aerodynamic acoustic-particulate-fluid systems for environment protection, energy fuel conversion, and industrial production.

Introduction

The shift, aggregation, deposition, removal, and suspension of numerous small particulates in air belong to the collective behavior processes of particulate-fluid systems. In terms of the particulates of sizes from several nanometers to several hundreds of microns, these processes have specific meaning in the field of particuology relating to environmental protection, the energy fuel conversion, and industrial production (Andrade, 1931; Brandt, 1989, 2001; Melde, Mark, Qiu, & Fischer, 2016; Qiao et al., 2020; Qiao et al., 2020; Yan, Lin, Zhao, & Chen, 2018; Zhang et al., 2020; Zhou et al., 2017). Taking the industrial smoke emission sources as an example, as many small particulates (such as $PM_{2.5}$, submicron particles, and nanoparticles) as possible are expected to be completely removed, as the requirements for greater air quality increase (He, Luo, Lu, Liu, & Fang, 2019). However, the trapping efficiency of a cyclone dust extractor for $PM_{2.5}$ is no higher than 40%, and that of a traditional electrostatic precipitator for submicron particles is no higher than 30% (Kilikevičienė et al., 2020). Particulate matter easily collects viruses and toxic heavy metals suspended in air, threatening human health (Pui, Chen, & Zuo, 2014). A fluid-particle system under the effect of an acoustic field may exhibit diverse phenomena, such as particle suspension, agglomeration, separation, aggregation, and fragmentation. These phenomena are of significance in both science and technology fields. When neglecting the challenge of particle fragmentation, acoustic-particulate technology generally has the advantage of high-efficiency removal of smoke particulates (Lee, Cheng, & Shaw, 1982; Shi et al., 2020). The application of a particulate acoustic fluid system is considered an important particle pollution treatment method (Andrade, 1931). The extensively experimental and computational visualization and analysis of a novel acoustic-particulate system should be able to overcome the challenge of a

* Corresponding author at: College of Energy and Power Engineering, Nanjing Institute of Technology, Nanjing 211167, China.
E-mail address: qiaozhenghui@njit.edu.cn (Z. Qiao).

https://doi.org/10.1016/j.partic.2020.11.009
1674-2001/

Nomenclature

A	Ke location point
AN	Abbreviation of anti-node
B	Ke location point
C	Ke location point
c_a	Acoustic velocit (m/s)
d_p	Diameter of particle (m)
D	Width of stripe spacing (m)
D_{es}	Distance of two identical particles (m)
f	Frequenc of sound (Hz)
F^d	Drag force (N)
F^{rad}	Acoustic radiation force (N)
F^S	Secondar radiation force (N)
H	Height of stripe (m)
k	Wave number (1/m)
K–K	Local view of x–z plane
N	Abbreviation of node
O	Center point of circular tube
OB	Line segment
p	Sound pressure (Pa)
P	Sound pressure amplitude (Pa)
ΔP	Variation of squeezed pressure (Pa)
Q	Length of aggregate cluster (m)
t	Time (s)
T	Time ccle of acoustic field (s)
v	Vibration velocit of particle (m)
V	Volume of particle (m^3)
ΔV	Variation of volume (m^3)
x	Position (m)
x–z	Cartesian coordinate system
α	Deviated angle of particle aggregation zone (–)
β_a	Compressibilit of fluid medium (1/Pa)
β_p	Compressibilit of particle (1/Pa)
μ	Viscosit coefficient of air (Pa s)
θ	Intersection angle (rad)
ρ	Densit of fluid medium (kg/m^3)
ρ_p	Densit of particle (kg/m^3)
λ	Wavelength (m)
Φ	Acoustic contrast factor (–)
ω	Angular velocit (rad)

traditional dust removal method for $PM_{2.5}$ (Andrade, 1931; Fan, Xu, Zhang, & Su, 2019; Hirayama, Plasencia, Masuda, & Subramanian, 2019; Kielpinski, 2015; Neild, 2016; Qiao, Dong, Huang, & Naso, 2018; Scales & Snieder, 1999; Zhang et al., 2018; Zhou et al., 2016).

For the application of particle-fluid systems, the geometric structures of particulate technology devices (such as a coal burning boiler or industrial dust catcher) are generally important and diverse (Guo, Chen, Shen, Wang, & Yang, 2020; Havey, Jaquay, Holton, Hussain, & Olenick, 2018; Sun, Yang, Wu, & Wu, 2020). The influence of different acoustic geometries on the motion behavior of particulate matter plays an important role in the technical development process of the acoustic aggregation process (Gallego-Juarez et al., 1999; Wang et al., 2018; Zheng, Li, Wan, Hong, & Wang, 2019). For example, Zhang's team has generally selected a one-dimensional vertical tube as a particulate aggregation chamber used for fire-smoke elimination (Zhang et al., 2020) and submicron coal-fired particle removal (Zhang et al., 2018). Based on a quadrilateral aggregation chamber (Qiao, Huang, Vincenzo, & Dong, 2015), Qiao's team (Qiao et al., 2020) found the tuning effectiveness of a normal 16-sided two-dimensional horizontal waveguide on smog aerosol aggregation. In addition, Gubaidullin's team (Gubaidullin, Ossipov, & Abdyushev, 2018) numerically determined the acoustically modulated dynamic distribution of the hyperbolic resonator on the aerosol particle drift process in a two-dimensional channel with a complex geometry. Vainshtein's team (Vainshtein & Shapiro, 2011) found the collective gathering of a quadrupole hyperbolical acoustic chamber on submicron particles in a three-dimensional configuration. Differing from the previous acoustic particle-fluid systems, an annular circular-tube waveguide used to enrich the particulate technology application is focused on in this study. Visualizing and analyzing the collective aggregation behavior of a particle system in an annular inhomogeneous acoustic field is the study objective of this paper.

For the development of a theoretical mechanism, it is gradually recognized that the aggregation kernel model (Zheng et al., 2019), the acoustic radiation force model (Qiao et al., 2015), and the secondary radiation force model (Qiao, Huang, Naso, & Dong, 2017) are three completely different types of main mechanisms. In previous outstanding studies (Shi et al., 2020; Yan et al., 2018; Zhang et al., 2018, 2020; Zheng et al., 2019), the aggregation kernel model is generally considered as the dominant mechanism to illustrate the aggregation characteristic of small particulates with different size ranges. This mechanism mainly focuses on the effective collision regulation of particulates with different sizes in an acoustic field environment. An effective collision causes two or more small particulates to grow into one large particulate (Zhang et al., 2018). However, under the condition of a strengthened acoustic field, the effective collisions are suppressed. The aggregation mechanism, which is particularly used for explaining the fragmentation phenomenon, still needs to be further studied (Shen, Huang, He, Zhang, & An, 2018). In addition, our previous studies (Qiao et al., 2017a, 2015; Qiao et al., 2018, 2020) preliminarily indicated that the acoustic radiation force and secondary radiation force belong to the dominant mechanism. Further, exploring the capability of the two forces in modeling the acoustic aggregation and fragmentation process is also a study objective.

In the current study, the acoustic (Liu et al., 2009), particle (Yan et al., 2018; Zhang et al., 2018), and operating (Qiao et al., 2018, 2020) parameters of a device are considered to be three types of main control parameters influencing the modulated effect of particulate shift, aggregation, deposition, and removal. The acoustic parameters mainly consist of the acoustic frequency (Andrade, 1931), sound pressure (Gallego-Juarez et al., 1999), inhomogeneous structure of an acoustic wave packet (Qiao et al., 2015), and resonance (Kilikevičienė et al., 2020). For the generally selected values, the acoustic frequencies are of low frequency, such as 0.7–3 kHz (Liu et al., 2009), 1.5 kHz (Zhang et al., 2020), 1.2 kHz (Andrade, 1931), and 2 kHz (Yan, Chen, & Li, 2016). The sound pressure is 63–502 Pa (Chen et al., 2015; Liu et al., 2009), 632 Pa (Liu, Wang, Zhang, Zhou, & Cen, 2011), and 282 Pa (He et al., 2019). The particle parameters mainly consist of the size distribution (Yuen, Fu, & Chao, 2017; Zhou et al., 2016), concentration (Zhang et al., 2020), viscosity (Zhang et al., 2018), and humidity (Yan et al., 2016, 2018). The operating parameters mainly consist of the phase (Qiao et al., 2015), the number of operating acoustic sources (Qiao et al., 2020), the residence time (Chen et al., 2015), the environmental temperature (Qiao et al., 2018), and the corona field (He et al., 2019). However, for practical aggregated particulates, the stacking density of particulates in the above studies is not referenced, and the density of the entity is utilized. For an acoustic field with a low frequency of 2 kHz and an environmental temperature of 20 °C, the wavelength (340 m/s ÷ 2000 Hz = 340 mm) is substantially larger than the aerodynamic suspension particles. The regular void structure (such as the porous characteristic (Qiao et al., 2018; Shi et al., 2020; Xu et al., 2019)) of particulates produced during the combustion process indicates that the stacking density should not be neglected. For two mini-sized particles with the same external contour volume, one solid substance and one porous substance have the same

external acoustic radiation area (Gor'Kov, 1962; Laurell, Petersson, & Nilsson, 2007; Xu et al., 2019). In the theoretical model of acoustic aggregation, the originally utilized particle density should be the stacking density rather than the entity density, particularly for biomass-fired smoke particulates.

Differing from our previous studies, the particulate aggregation and fragmentation in a novel annular one-dimensional acoustic field with a resonant frequency range of 0.12–1.9 kHz and a sound pressure amplitude range of ≤1000 Pa are studied here. Based on the wave engineering concept of parity-time symmetry (Fleury, Sounas, & Alu, 2015; Qiao et al., 2017a; Scales & Snieder, 1999; Sirtori, Barbieri, & Colombelli, 2013; Strecker, Partridge, Truscott, & Hulet, 2002), the annular circular-tube waveguide coupled with the two same Helmholtz sound sources (HSSs) contrarily installed at the tube ends is an attempt to generate the acoustic field environment. The complex acoustic-particulate process within the waveguide belongs to a novel particle-fluid system. The three mechanisms corresponding to the acoustic radiation force, secondary radiation force, and stripe models are attempts to theoretically illustrate the acoustic aggregation phenomenon of rice-husk fired smoke particulates with a size range of 36.7 nm–840 μm. The complex aggregation and fragmentation process of particulates between the contiguous node and anti-node within a wave packet is discovered through both experiments and calculations. This complex process should be attributable to the characteristic change in the particle physical parameters (such as the size, staking density, and porosity) caused by the different pressure strengths of an acoustic field. The three types of main control parameters, including acoustic, particle, and operating parameters of the device have been carefully discussed. The balanced modulation of two radiation forces is provided to explain the process control, which is extremely important for the engineering design of an acoustic-particulate-fluid system. The visualization and analysis of the acoustic-particulate system in an air medium enhances the application of particle technology broadly relevant to environment protection, energy fuel conversion, and industrial production. This paper is another meaningful contribution to the authors' previous series of studies (Powder Tech., 2015; Powder Tech., 2017; Powder Tech., 2020).

Setup and method

Fig. 1(a) shows the design and operation principle of the experimental setup and its measurement method. For the design, the two same HSSs based on the parity-time symmetry (Fleury et al., 2015; Qiao, Huang, Naso, & Dong, 2017) are contrarily installed at the ends of annular circular-tube waveguide along the center line, and each HSS consists of a Helmholtz resonator and a speaker. The waveguide length of the annular circular-tube centerline is 978 mm, and the internal diameter is 35 mm (Qiao, Huang, & Dong, 2014). The material of the circular tube is transparent plexiglass. The geometric sizes of the HSS satisfy the resonant similarity principle (Cheng, Dong, & Qiao, 2016), where the resonant frequency of the Helmholtz resonator equals the seventh-order harmonic frequency of 1.286 kHz of the waveguide. The component arrangement results in a complex generation device with an annular acoustic field environment. For the operation, a strengthened annular one-dimensional acoustic field is motivated by the sinusoidal audio energy of two speakers (8Ω) supplied with a power amplifier and a signal generator. For the field measurement of an acoustic quarter-wavelength of larger than 6 cm, sound pressure meters are chosen to weight the gradient structure of an inhomogeneous acoustic field. The measurement positions x_i (i = 1–55) from among the 55 positions are uniformly arranged along the circumferential length direction of the annular waveguide, and x_{28} = 48.9 cm is the middle position. The positions x_i with an even numbered subscript are 27 equal points on the waveguide, and the other x_i are the measurement positions 15 mm away from each position for which the subscript i is an integer multiple of 4.

To easily understand the acoustic field environment (Qiao et al., 2020), a fluid simulation using *ANSYS* acoustic scientific software is applied to calculate the pressure fluctuation regulation of the acoustic field. Fig. 1(a) shows the numerical model of the fluid medium of air within a circular tube. The mesh size of the finite element simulation is sufficiently accurate at much smaller than 1/8 wavelength. For the boundary conditions, the horizontal side of the waveguide is rigid, and the two ends correspond to a pressure variation of a sinusoidal form with the same amplitude and frequency.

For the acoustic experiment of particle aggregation, the fired smoke particulate matter with a main size of less than 0.84 mm is loaded into the waveguide to display the particle aggregation in an annular acoustic field. One specific camera is used to record the aggregation effect in space-time. The experimental material type of the particle source is the coke particulate of rice-husk fired smoke. With a specific particle sieve, the measured equivalent diameter ranges of the particle weight percentage are <100 μm (33%), 150–100 μm (13.25%), 180–150 μm (17.95%), 212–180 μm (7.6%), 212–250 μm (15.67%), 250–297 μm (6.9%), 297–420 μm (0.2%), 420–590 μm (4.42%), 590–840 μm (0.97%), and >840 μm (0.1%). The key point O is the center of the circular tube, and the other key points A, B, and C correspond to three characteristic locations. In addition, α represents the acoustically deviated angle of the particle aggregation zone far from the line segment OB.

Mechanisms

In an acoustics-particle-fluid system under a standing wave environment, it is believed that the acoustic radiation force and the secondary radiation force play an important role in the shift and aggregation evolution process of the particulates (Laurell et al., 2007). These two types of force mechanisms are effective for particulates of a size much smaller than the wavelength of an acoustic field. However, the balance modulation of two forces on the particle characteristics (size and stack density) has not been considered as the control mechanism of the particle system. This control mechanism is the quantitative contribution of the present paper.

Acoustic radiation force

In the fluid medium of air, a small coke-type particulate with size much smaller the wavelength 340 mm can equal a spherical particle in terms of compressibility. The action of a one-dimensional acoustic standing wave on a single compressible sphere is called the acoustic radiation force, as first suggested by Gor'kov (Gor'Kov, 1962). The action force formula is expressed as follows (Brandt, 2001; Bruus, 2012; Qiao et al., 2015):

$$F^{\mathrm{rad}} = -\left(\frac{\pi^2 P^2 \beta_a}{12\lambda}\right) d_{\mathrm{p}}^3 \Phi(\beta, \rho) \sin(2kx), \tag{1a}$$

$$\text{and} \quad \Phi(\beta, \rho) = \frac{5\rho_{\mathrm{p}} - 2\rho_{\mathrm{a}}}{2\rho_{\mathrm{p}} + \rho_{\mathrm{a}}} - \frac{\beta_{\mathrm{p}}}{\beta_{\mathrm{a}}}. \tag{1b}$$

Here $k = 2\pi f/c_{\mathrm{a}}$ represents the wave number; P, f, and x represent the sound pressure amplitude, the frequency, and the position of acoustic field, respectively; ρ_{a}, $\beta_{\mathrm{a}} = 1/\left(\rho c_{\mathrm{a}}^2\right)$, and c_{a} represent the density, compressibility, and acoustic velocity of a fluid medium; ρ_{p}, $\beta_{\mathrm{p}} = -(1/V)(\Delta V/\Delta P)$, and d_{p} represent the density, compressibility, and particle diameter; V represents the volume of the particle; and ΔV represents the variation of V with the variation of ΔP under squeezing pressure. In addition, $\Phi(\rho,\beta)$ represents the

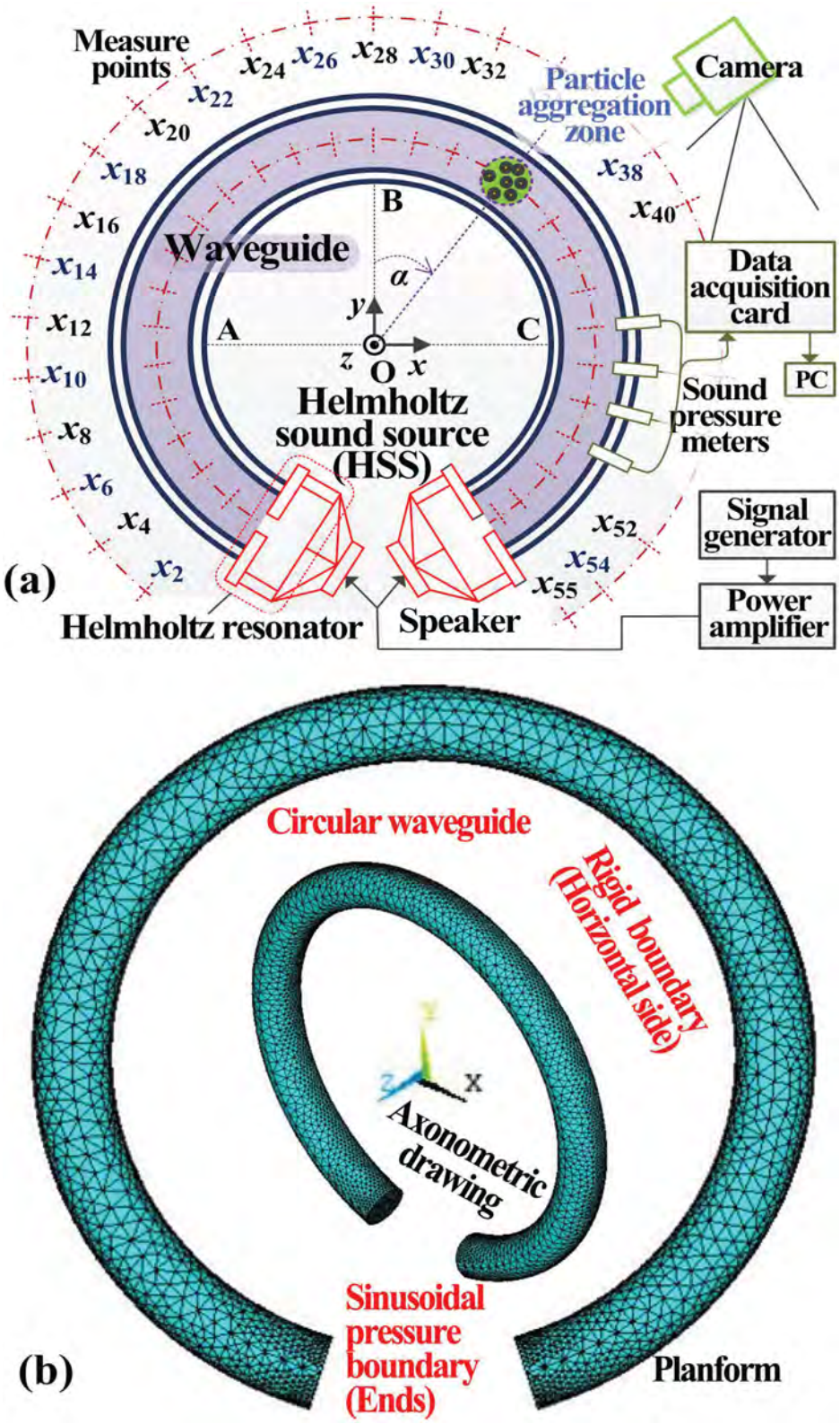

Fig. 1. Diagrammatic sketch of setup and model: (a) experiment and (b) simulation.

acoustic contrast factor. The value of Φ depends on the density-compressibility characteristic of the particle and fluid medium. When $\Phi < 0$ (or $\Phi > 0$), the particles shift toward the pressure anti-node (or node) of the standing wave. The value of F^{rad} indicates the shift extent of particles between any contiguous anti-node and node. Owing to the particle size diversity of rice-husk fired smoke, a different shift velocity of the coke particulates causes a complex particulate collision aggregation effect.

Secondary radiation force

Different from the particle shift between the inhomogeneous structures of the acoustic field, the secondary radiation force represents the acoustically interactive force between any two particles. This force indicates the aggregation extent of any two particles, regardless of whether their sizes are the same. In addition to the acoustics-particle characteristic, the force formula also contains the position relationship of the intersection angle between the central line of two particles and the propagation direction of an acoustic field, as follows (Ahn et al., 2014; Laurell et al., 2007; Qiao et al., 2017a):

$$F^s = \frac{\pi d_p^6}{16}\left[\frac{(\rho_p-\rho_a)^2(3\cos^2\theta-1)}{6\rho_a D^4}v^2(x) - \omega^2\rho_a\frac{\beta_p-\beta_a}{9D^2}p^2(x)\right] \quad (2)$$

Here θ represents the intersection angle; D represents the distance of two identical particulates; $\omega = 2\pi f$ represents the angular velocity of a fluid medium; and $v(x) = p(x)/(\rho_a c_a)$ and $p(x)$ represent the particle vibration velocity and the sound pressure of the acoustic field, respectively. Owing to the inhomogeneous structures of a standing wave, the two terms with equal signs on the right side of Eq. (2) demonstrate a different particulate aggregation regulation in an anti-node and a node. At the positions near the pressure anti-node where $v(x) = 0$, the secondary radiation force F^s is attractive. At the positions near the pressure node where $p(x) = 0$, the value of F^s depends on the value of θ. If $\theta = 0$, F^s is repulsive; by contrast, if $\theta = 90^o$, F^s is attractive. When $v(x) = 0$, or $p(x) = 0$ and $\theta = 90^o$, the attractive force enhances the aggregation process of two coke particulates. By contrast, when $p(x) = 0$ and $\theta = 0$, the repulsive force enhances the aggregation and fragmentation process in the direction parallel to the propagation direction of an acoustic field. For two particles with similar sizes, Eq. (2) corresponding to one simplified expression is convenient and effective during the calculation, particularly for the same-sized particles. For polydisperse particles, the expression of ${d_p}^6$ should be replaced by ${d_{p1}}^3 \cdot {d_{p2}}^3$ (the third powder of the product of two particle diameters, d_{p1} and d_{p2}) (Weiser, Apfel, & Neppiras, 1984). To an extent, the effect of the size difference on the particle aggregation can be analyzed on the basis of Eq. (2).

Stripe

Based on two radiation forces, the equilibrium spacing D of two particles (where $dD/dt = 0$, and t is time) can be derived when simultaneously considering the drag force F^d on the particles (Weiser et al., 1984). Here, $F^d = 3\pi\mu d_p dD/dt$, where μ is the viscosity coefficient of air. The three types of forces form a relatively balanced relation for two moving particles with the same size in a one-dimensional acoustic standing wave field. The theoretical equilibrium spacing D_{es} can be calculated using the stripe model of Weiser (Qiao et al., 2017a; Weiser et al., 1984) as follows:

$$D_{es}^6 = \frac{d_p^3}{4k^3}\left(\frac{\rho_p}{\rho_a}-1\right)^2\left(\frac{\rho_p}{\rho_a}-\frac{\beta_p}{\beta_a}\right)^{-1}. \quad (3)$$

Eq. (3) demonstrates that the equilibrium spacing of a large number of particles evolves into many parallel stripes consisting of a particle aggregation cluster, when the acoustic action time is sufficient long.

Results and analysis

Acoustic field and radiation force calculation

Fig. 2 shows the characteristics of the acoustic field during the process of particulate aggregation. The resonant effects are clear at 0.12, 0.2, 0.52, 0.8, 1.1, 1.3, 1.6, and 1.9 kHz (see Fig. 2(a)). The sound pressure increases with the input voltage and decreases with the resonant frequency (Fig. 2(b)). The sound pressure amplitude at a certain input voltage amplitude can be acquired by the range relation of the pressure and a voltage of 1–10 V. The experimental resonant frequency of 1.3 kHz is similar to the designed value of 1.286 kHz. The experimental and theoretical harmonic effects of the waveguide are always similar in the resonant frequencies (see Fig. 2(c)). According to Eq. (1b), the variations in the acoustic contrast factor with the density and the compressibility of the particulates is calculated. The monotonous variation (see Fig. 2(d)) demonstrates that the shift and accumulation of coke particulates between the anti-nodes and nodes of a standing wave are overwhelmingly affected by the physical characteristics of the smoke particles.

Fig. 3 shows the macro- and micro-structures of coke particles at four magnifications under a scanning electron microscope (SEM). The particle size distribution (36.7–840 μm) can be given through the number statistics of the SEM photos. It can be seen that small particulates with an external surface size of approximately 857.1 μm (length) and 135.2 μm (width) mainly appear as hollow cylinders with a wall thickness of approximately 49.95 μm (see Fig. 3(a)). As an example, in terms of the inner surface, the detailed structure appears as numerous stripe fins with a thickness of approximately 970.8–1.996 μm (see Fig. 3(b)). The interspacing between two contiguous fins is approximately 6.817–10.76 μm. Combined with alveolus details (see Fig. 3(c)), the surface of the fins fills in regularly with a porous aperture of approximately 1.134–3.86 μm. The material of the fins consists of numerous nano particles with a size of approximately 36.7–307.4 nm (see Fig. 3(d)). The actual density of the hollow cylindrical particulate should be less than the density of the ideal solid carbon particles generally considered in a previous study (Karpul, Tapson, Rapson, Jongens, & Cohen, 2010), where $\Phi \approx 2.5$ ($\beta_p = 1.99 \times 10^{-5}$ Pa^{-1}, $\rho_a = 1.21$ kg/m^3, $\rho_p = 2200$ kg/m^3, $\beta_a = 7.15 \times 10^{-6}$ Pa^{-1}). Regardless of whether the potential measurement error of the particle sieve on the cylindrical particles is neglected, it is reasonable to focus on the coke particle density range of 1.21–2200 kg/m^3 in Fig. 2(d).

As an example, the inhomogeneous characteristic of a one-dimensional acoustic field is demonstrated in Fig. 4. The pressure distributions of 0.191 and 0.52 kHz display an inhomogeneous-acoustic gradient structure within an annular waveguide. The pressure curves with a measuring time interval of 10 ns constitute the standing wave patterns (Qiao et al., 2017a) with one and three wave-packets (see Fig. 4(a) and (c)). The experimental fluctuation pattern of the wave-packet along the annular direction agrees perfectly with the stimulation results (see Fig. 4(b) and (d)). Combined with Eq. (1a), the inhomogeneous acoustic field provides the acoustic fluid environment of the collective motion and accumulation behavior process of the coke particulates. Further, based on Eq. (2), the interactive force between particles is calculated. The constants are $\beta_p = 1.99 \times 10^{-5}$ Pa^{-1}, $\rho_a = 1.21$ kg/m^3, $\rho_p = 164$ kg/m^3, $c_a = 340$ m/s, $\beta_a = 7.15 \times 10^{-6}$ Pa^{-1}, $f = 0.191$ kHz, and $\Phi \approx -0.3$. In the direction of $\theta = 0^\circ$ and $\theta = 90^\circ$, the repulsive and attractive forces increase simultaneously with the increases in the particle diameter and sound pressure (see Fig. 5). Conversely, they decrease clearly with an increase in the inter particle distance.

When $\sin(2kx) = 1$, the calculated acoustic radiation force for $\Phi > 0$ and $\Phi < 0$ is shown in Fig. 6(a). It can be seen that the positive (respectively negative) range of F^{rad} is 10^{-21} N to 10^{-2} N (respectively -10^{-20} N to -10^{-2} N) for a particle diameter of 1 μm to 0.1 m. The absolute value ranges are simultaneously contained within the F^s value ranges of the repulsive force (10^{-30}–10^{33} N) and the attractive force (10^{-35}–10^{34} N) (see Fig. 5). The dominant force alternation depends on the characteristic change in particles (such as β_p, ρ_p, d_p, D, and θ) and the acoustic field (such as $p(x)$, P, f). The

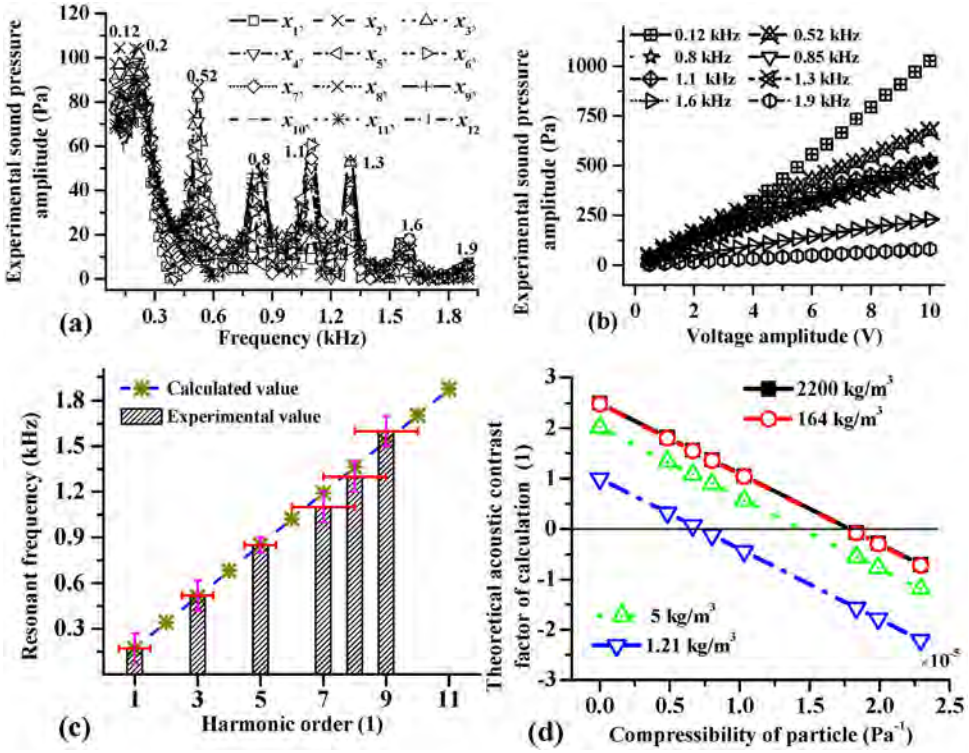

Fig. 2. Acoustic characteristics: (a) experimental frequency response, (b) experimental relation between sound pressure and voltage, (c) resonance, and (d) theoretical acoustic contrast factor of the calculation.

drag force balance of F^{rad} and F^{s} on the particulates results in a static stripe of a particle cluster (Weiser et al., 1984). Based on Eq. (3), the calculated stripe spacing is shown in Fig. 6(b). As an example, for a particulate diameter of approximately 20 μm, the stripe spacing of the particulates amplifies monotonously from 2.5 to 8 mm with a decrease in the acoustic frequency from 1.3 to 0.12 kHz. Within this frequency range, the further increase in the stripe spacing is only attributed to the aggregate size increase of the particulates.

Aggregation evolution with different frequencies

Fig. 7 shows the collective behavior of particulate evolution with frequency under the condition of the same input voltage amplitude of 10 V. It can be seen that the particulate aggregation effect is clearly different at different resonant frequencies. At low frequencies (0.191 and 0.52 kHz), the aggregate clusters (see Fig. 7(b) and (c)) are mainly shifted and accumulated toward the pressure anti-node of the acoustic field (see Fig. 4). The aggregation should be attributed to the predominant acoustic radiation force, which is closely related to the pressure time–space fluctuation structure (wave-packets) at low frequencies. At high frequencies (0.8 kHz and 1.3 kHz), numerous stripes of particulate aggregation are distributed on the pressure nodes of the acoustic field. The experimental values of stripe spacing are similar to the theoretical values (see Fig. 6(b)). The spacing values of 6.4 mm (0.191 kHz), 3.25 mm (0.8 kHz), 2.5 mm (1.3 kHz), and 8 mm (0.12 kHz, see Fig. 8(l)) always coincide experimentally and theoretically. The spacing control range (2.5–3.8 cm) is much larger than our previous stripe-spacing findings (400–800 μm) of tobacco-fired smoke-aerosol particle manipulation (Qiao et al., 2017a). In terms of the particle size range (<100 μm) with the largest weight percentage (33%), the predominant size of the coke particulates, approximately 20 μm, indicates a new size measurement technique for aerodynamic suspended micro-particles. In addition, the geometry of a stripe has an umbrella shape along the vertical direction (see Fig. 7(b)). The bottom and top of the "umbrella" respectively correspond to the maximal and minimal values of the stripe spacing. The two values result from the predominant diameter of the particulates. Combined with the data in Fig. 6(b), the maximal value of 21.5 mm (d_p = 250 μm) and the minimum value of 6.4 mm (d_p = 20 μm) limit the stripe spacing range for the particulates (87.47%) of 20–250 μm within a resonant frequency of 0.191 kHz.

As an example, Fig. 8 shows the stripe details at different frequencies and sound pressure amplitudes. Within the error range of the harmonic frequency of the fifth-order, even though the spacing width of the stripe changes is weak, the thickness and height still clearly change. The shape of the stripe is displayed as a thin film with a thickness of approximately 0.3 mm. In practical terms, one individual striped thin-film belongs to a regular particulate aggregation cluster.

Aggregation evolution with different sound pressure amplitudes

Fig. 9 (vertical view) shows the characteristic behavior of the particulate evolution with a sound pressure amplitude under the condition of the same acoustic frequency of 0.191 kHz. It can be seen that the initial states of the particulates are uniformly distributed on the inner-wall surface of the waveguide bottom (see Fig. 9(a)) because of Earth's gravity. With an increase in the input voltage amplitude, two types of radiation forces gradually increase, and the originally static particles gradually remove the gravity. The particulates of sizes from small to large gradually begin to move and suspend in the air in the form of a stripe. The number of particles attached to the inner wall gradually decreases with an increase in the pressure amplitude, and the spacing value of the stripes also gradually increases (see Fig. 9(b)–(k)). Combined with the theoretical regulation shown in Fig. 6(b), the spacing enlargement with the sound pressure should be attributed to the size enlargement of growing particles in the small stripe parti-

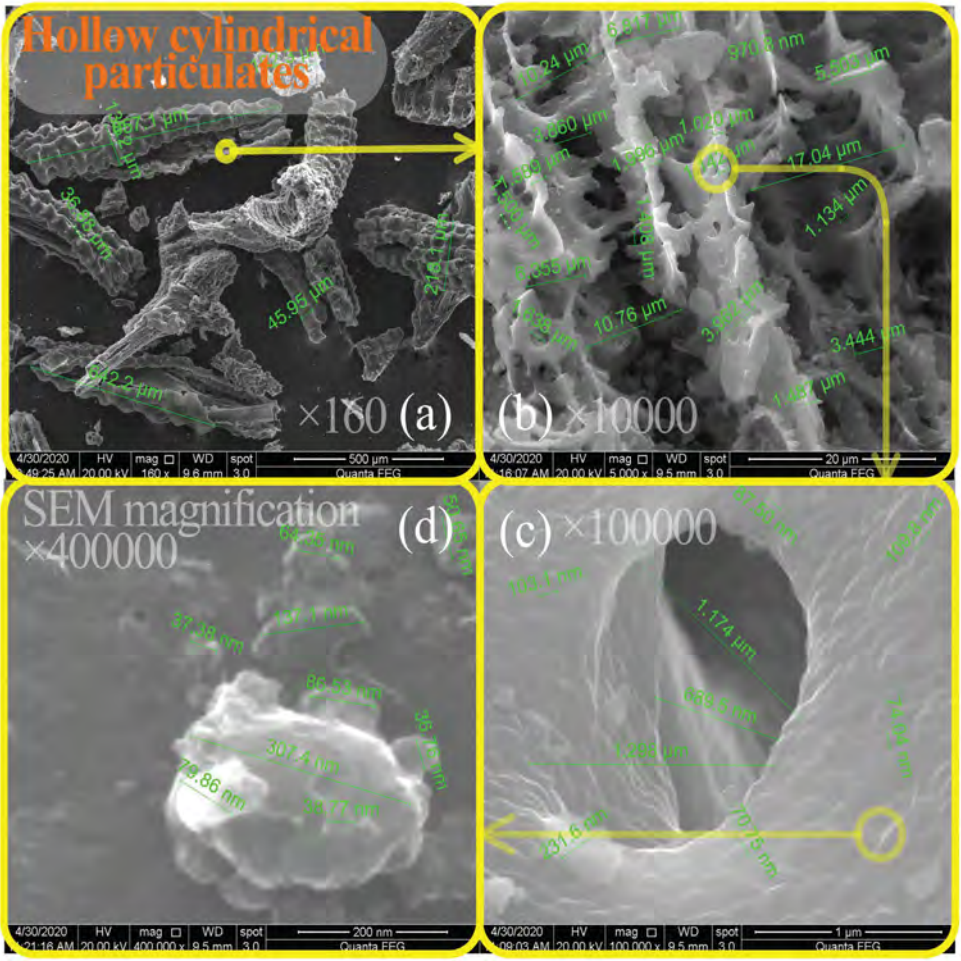

Fig. 3. SEM details of particulates. (a)–(d) refer to different magnifications.

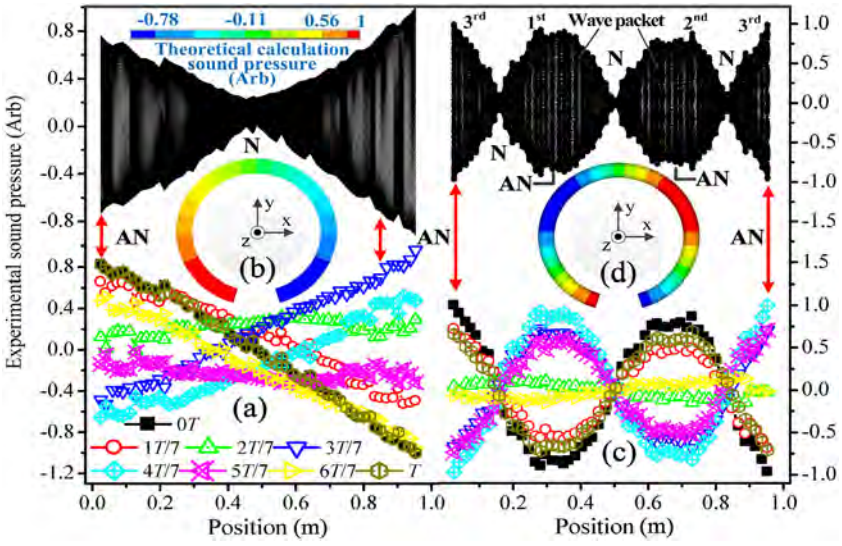

Fig. 4. Sound pressure distribution: (a) and (b) refer to 0.191 kHz; (d) and (c) refer to 0.52 kHz; (a) and (c) are experimental data; (b) and (d) are theoretical calculated data; and AN and N respectively represent the anti-node and node of a standing wave.

cle cluster. The experimental range (approximately 2.75–36.7 mm) of the spacing enlargement agrees similarly with the theoretical range of 2.5–38 mm. The theoretical maximum (38 mm) should be attributed to particles with the largest experimental size of $d_p \approx 840$ μm.

As an example, Fig. 10 (front view) shows the behavioral characteristics of the particulate stripe evolution (0.191 kHz) along the vertical direction. It can be seen that the height and width of the stripe gradually and simultaneously increase with the rise in the sound pressure amplitude. There experimentally exits an obvious

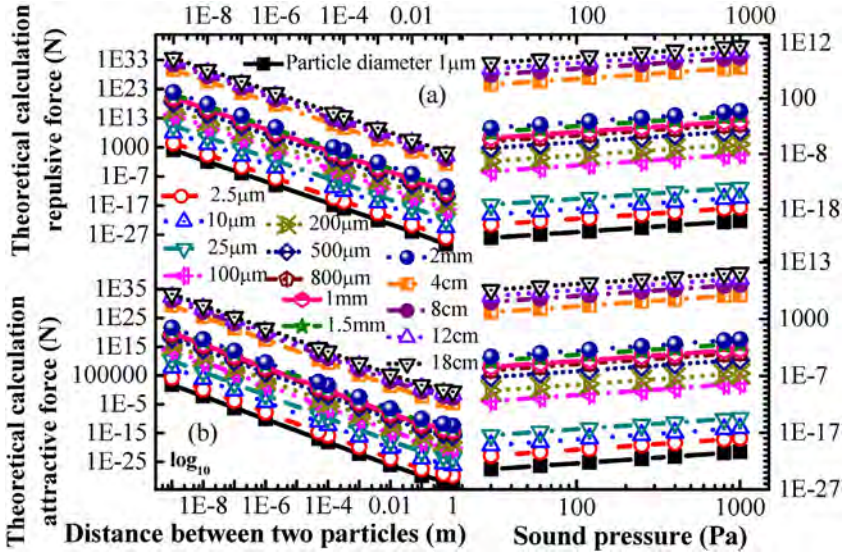

Fig. 5. Calculation of secondary radiation force: (a) $\theta = 0^{\circ}$, $p(x) = 120$ Pa; (b) $\theta = 90^{\circ}$, $p(x) = 120$ Pa; (c) $\theta = 0^{\circ}$, $D = 1$ mm; (d) $\theta = 90^{\circ}$, $D = 1$ mm.

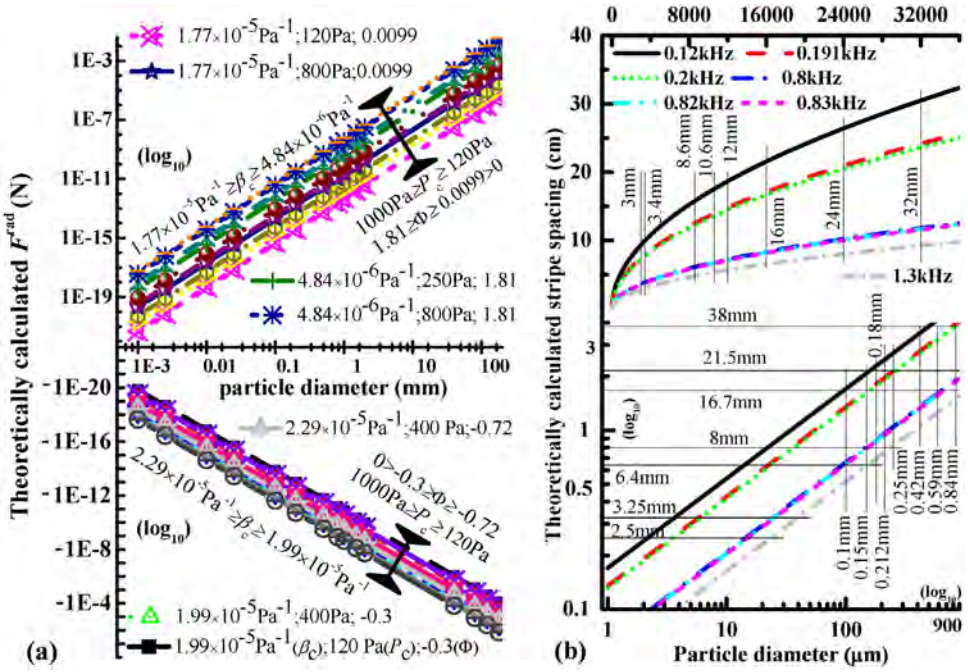

Fig. 6. Calculation of acoustic radiation force and stripe spacing: (a) and (b) respectively refer to the force and spacing.

height-value jump between two input voltage amplitudes of 6.5 and 7.5 V. This experimental characteristic might reveal two completely different acoustic action mechanisms. Combined with the positive-negative alternation of the acoustic contrast factor, the mechanism alternation might result from the change in the physical characteristic of the aggregated particulates during the growth process of a particle stripe.

Dynamical evolution of aggregation

Fig. 11 (front view) shows the dynamic periodic characteristic of the behavior evolution for a particulate stripe under the condition of an input voltage amplitude of 4 V and a frequency of 0.191 kHz. It can be seen that the particle distribution along the propagation direction of an acoustic wave changes periodically over time (cycle of approximately 1.056 s), and the stripe with the umbrella shape varies dynamically. As an example (see Fig. 11(b)–(l)), the umbrella size of the stripe cluster changes with the motion positions of the stripe particle cluster. Two larger repulsive forces caused by the large contiguous clusters (1 and 4) drive two small clusters (2 and 3) moving toward each other (see Fig. 11(b) and (c)). They then merge and become one new large cluster (2') (see Fig. 11(c) and (d)). When the cluster becomes sufficiently large, the repulsive forces between the inter particles within the top of the cluster become dominant. The dominant repulsive forces and gravity cause the inter particles to land at the contiguous bottom of the inner-surface of the waveguide. The landing particles accumulate into a growing new cluster (see Fig. 11(d)–(h)). The bottom distance between the new large cluster and the contiguous large origin cluster (such as 3' and 4', or 2' and 3', in Fig. 11(i) and (j)) is approximately 16.7 mm, and the top distance is approximately 4.7 mm (16.7–12 = 4.7). They all contain the theoretical range (2.5–38 mm) of the stripe spacing.

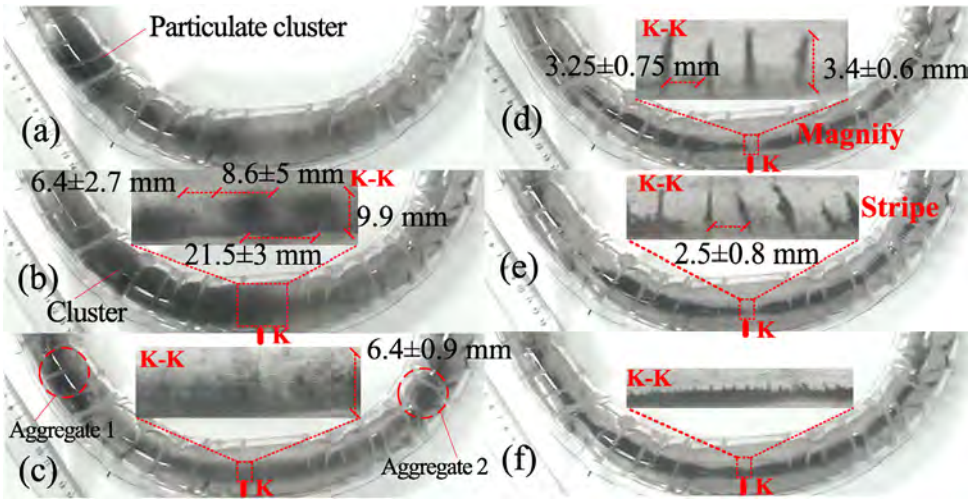

Fig. 7. Particulate distribution at six frequencies: (a) 0.12, (b) 0.191, (c) 0.52, (d) 0.8, (e) 1.3, and (f) 1.6 kHz; K-K represents the local view of the x-z plane.

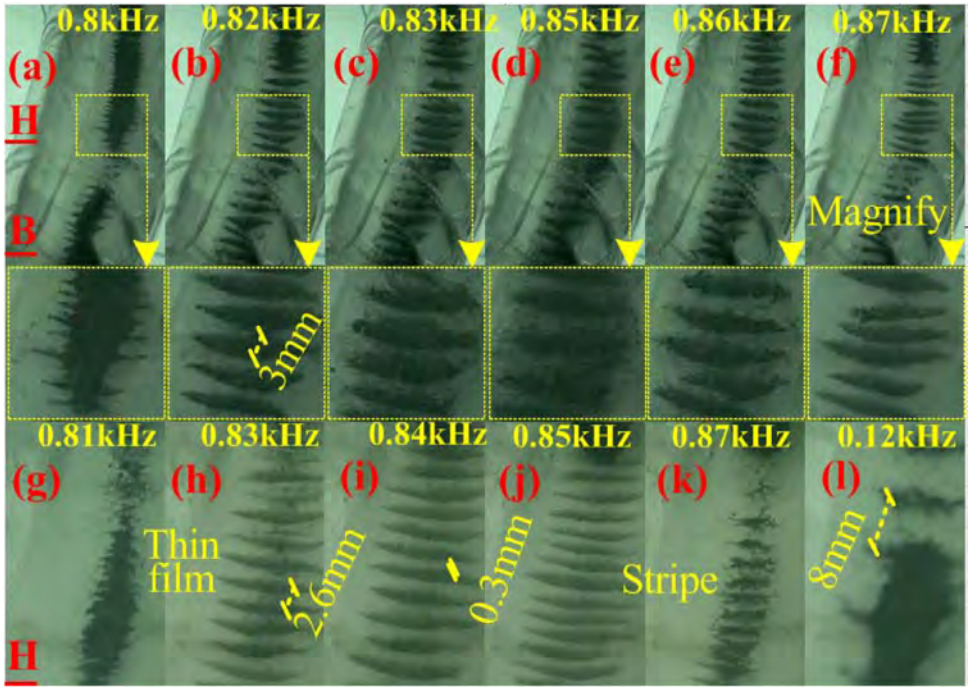

Fig. 8. Stripe details for nine frequencies. (a)–(f) Input voltage amplitude of 10 V; (g)–(l) input voltage amplitude of 4 V; the signs of B and H represent the specific positions of the waveguide.

The dynamic variation of an aggregate stripe should be attributed to the practical complexity of the physical dimensions of the coke particulates during the smoke production process. In terms of environment protection, the effective collisions of small particles such as air-pollution, $PM_{2.5}$, should be strengthened by applying the enhancement mechanism of a stripe-particle-cluster growth. The sufficiently large particles of the agglomeration can be removed using a cyclone dust extractor or electrostatic precipitator during the next stage (Kilikevičienė et al., 2020).

Fig. 12 (axonometric drawing) shows the dynamic periodic characteristics of the behavior evolution for an aggregate cluster under the conditions of an input voltage amplitude of 10 V and frequency of 0.191 kHz. It can be seen that the aggregate cluster periodically changes between the node and anti-node of the acoustic field. The volume of an aggregate cluster varies with time, and here, it is weighed by a defined length parameter Q. With same weight and number of origin particulates, a large Q corresponds to a large volume of aggregate clusters. The motion direction of the cluster alternates toward the node or anti-node depending on the acoustic contrast factor Φ relating to the physical characteristics of the aggregates. For specific initial particulates, such as generally ideal solid carbon particulates ($\Phi > 0$), the particulates migrating toward the pressure node constitute a specific aggregate cluster. There exists a maximal cluster volume, where $Q = 15$ cm (see Fig. 12(m)). During the migration process, two or several particulates merge into one new large aggregate, and its acoustic contrast factor decreases toward a value of less than zero. When $\Phi < 0$, the motion direction of the cluster turns into the pressure anti-node. The collision aggregation becomes violent owing to the increase in the number of particle pairs moving in the opposite direction. During the acoustic aggregation, the volume of the cluster gradually becomes small, and the distance of two contiguous particles

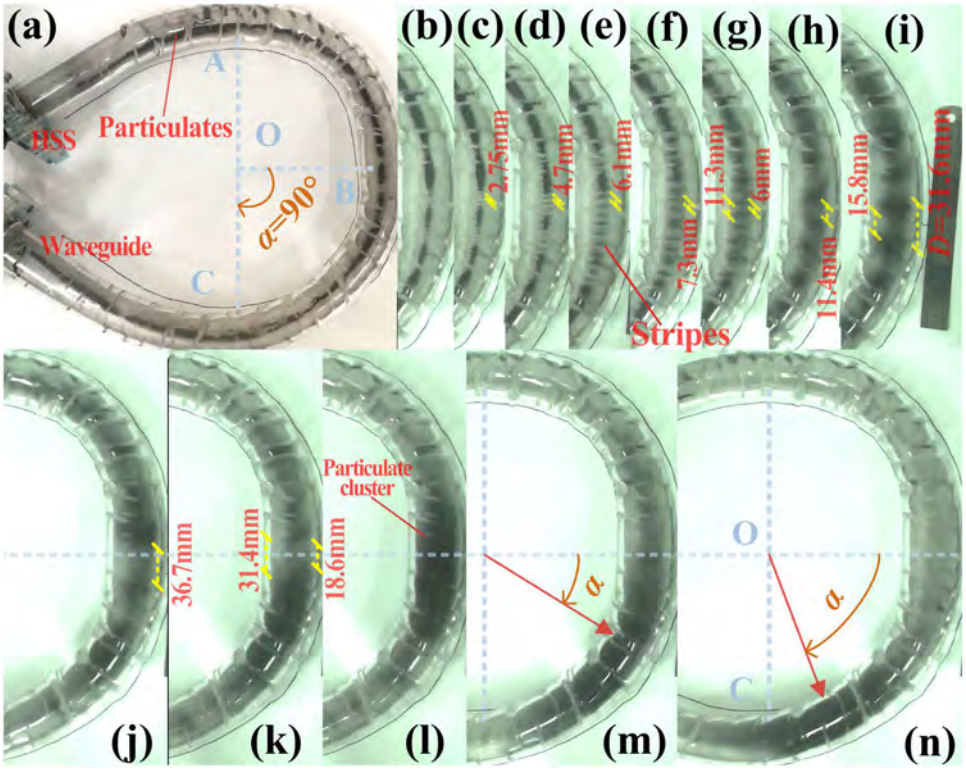

Fig. 9. Particulate distribution for 13 input voltage amplitudes: (a) 0, (b) 0.5, (c) 1, (d) 1.5, (e) 2, (f) 2.5, (g) 3, (h) 4, (i) 4.5, (j) 5.5, (k) 6.5, (l) 7.5, (m) 9, and (n) 10 V.

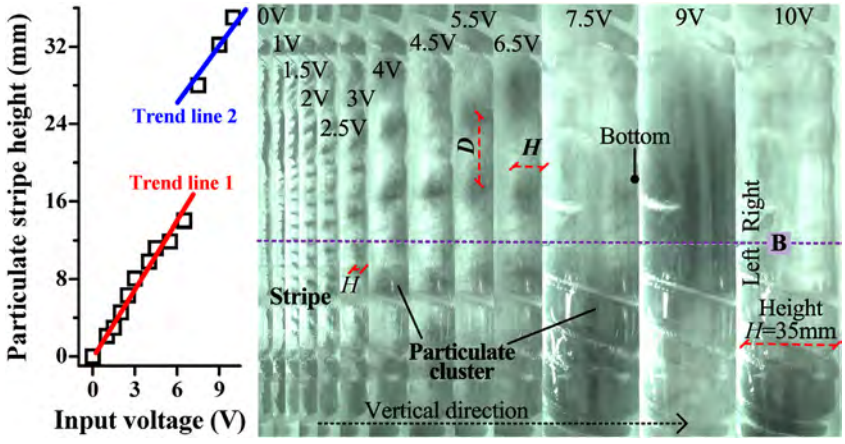

Fig. 10. Stripe particulate cluster characteristic. *H* and *D* represent the height of the stripe and the width of the stripe spacing, respectively.

also gradually decreases. Combining Figs. 5(a) and 6 (a), when the distance of two particles is sufficiently small, the repulsive force along the propagation direction of the acoustic wave will obviously increase and become dominant. At this moment, the cluster achieves the smallest volume, where $Q \approx 10$ cm (see Fig. 12(n)). After a short homeostasis of approximately 2 s, the sole cluster breaks up into two small clusters of $Q_1 \approx 7.8$ and $Q_2 \approx 5.6$ cm (see Fig. 12(o)) depending on the secondary radiation force. The spacing of the two clusters is approximately 2.8–3.8 cm (see Fig. 12(d), (g), (k), and (o)), similar to the theoretical calculation (see Fig. 6(b)). Then, the fragmentation of the aggregates becomes dominant, and the physical characteristic of the particulate results in $\Phi > 0$. Under the action of an acoustic radiation force, the particulates are moved to the pressure node of the acoustic field again. Accordingly, the dynamically and periodically collective particulate behavior suggests a novel particulate-fluid platform. This platform provides a contactless tunability fluidization process, which can be applied to many aspects such as a pulverized coal burner or particulate material production, among others.

Compared with our previous studies (Powder Tech., 2015; Powder Tech., 2017; Powder Tech., 2020), the experimental findings in this paper have abundant implications in terms of particle manipulation. The implications include new acoustic-particle-operating parameter-control methods, a new geometric device structure design, application of mechanisms for particle manipulation, and their selection.

Conclusions

Particulate aggregation through an inhomogenous one-dimensional acoustic field within an annular circular-tube waveguide was studied experimentally and theoretically under a

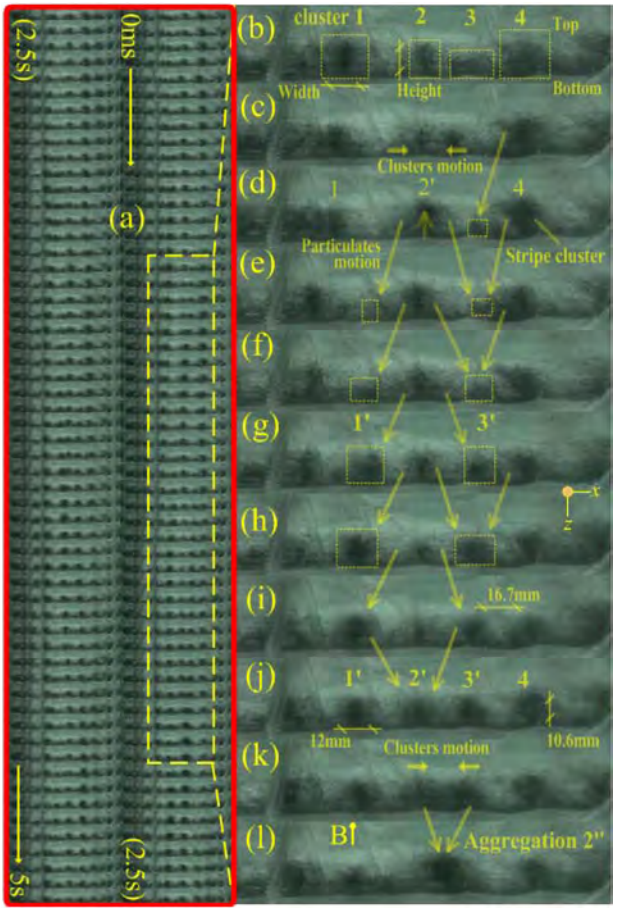

Fig. 11. Dynamic stripe at 4 V: (a) time interval of 44 ms of two adjacent images; (b)–(l) time interval of 132 ms of two adjacent figures. The sign of B represents the reference position.

resonant frequency range of 0.12–1.9 kHz. The particle interaction environment with a sound pressure of up to 1000 Pa is successfully modulated by a waveguide with an input power of 0–12.5 W. The experimental particulate source material is the coke particulate of rice-husk fired smoke of sizes no larger than 0.84 mm. The results found that the aerodynamic particulate aggregation behavior is extremely complex, which is collectively manipulated by the wave packet structure tuning of the inhomogenous acoustic field. A low sound pressure causes umbrella shaped dynamic particle stripes with a tunable weight, height, and spacing. A high sound pressure causes a dynamic particle aggregation cluster with a tunable volume and spacing. The dynamic evolution process of the particle stripes and particle clusters belongs to two obviously different phenomena regarding particulate aggregation and fragmentation. The balance tuning of the acoustic radiation force and secondary radiation force is analyzed as the control mechanism of the experimental phenomena. The control method is the physical characteristic (such as the size, the stacking density, and the porous) tuning of particulates under different acoustic environments. The results are extremely valuable for understanding the collective particle motion behavior of a standing wave acoustic field, particularly the aggregation, fragmentation, suspension, collision, deposition, removal, and transfer. The new findings enhance the application of a particulate-fluid system related to environmental protection, energy fuel conversion, and particulate material production, among other factors.

In addition, the new findings of this study indicate that there are many additional areas for future research. For example, (1) when modelling the particle aggregation, the cylindrical particles with pores as spheres are considered, which largely deviates from the actual particle shape. Commonly, the particle shape will affect the force acting on the particle, and thus affect the equilibrium position of the particles. However, the experimental values of stripe spacing agree well with the theoretical values. The effect of the particle shape should be further studied. (2) For modelling an acoustic particle interaction, the acoustic wake effect is often considered a

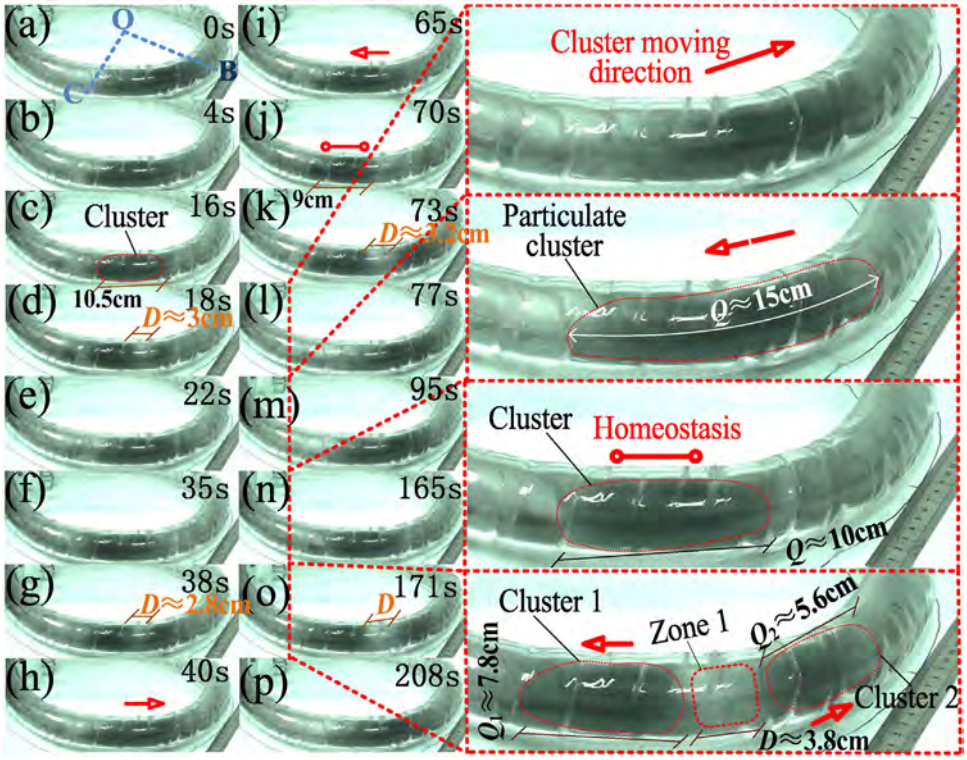

Fig. 12. Dynamic aggregate cluster at 10 V: (a)–(p) Evolution distribution at different moments.

major particle interaction mechanism. However, the acoustic wake effect is ignored in this study; nevertheless, the new phenomena are still appropriately explained based on the three mechanisms of the acoustic radiation force, secondary radiation force, and stripe models. Therefore, compared with general cognition, further research should be both subversive and complementary in terms of the research direction of an acoustic-particle-fluid system.

Declaration of competing interest

The authors declare that they have no conflicts of interest.

Acknowledgements

This paper was supported by the Natural Science Foundation of Jiangsu Province of China (Grant No. BK20191019), the Natural Science Research Project in Colleges and Universities in Jiangsu Province of China (Grant No. 19KJB470022), the Scientific Research Start-up Foundation funding of High-level Introduction Talents of Nanjing Institute of Technology (Grant No. YKJ201912), and the Open Fund Project of the Key Laboratory of Energy Thermal Conversion and Control of Ministry of Education of Southeast University.

References

Ahn, K. H., Ahn, J., Kim, I., Kang, S., Kim, S., Chu, K. H., et al. (2014). Separation of fine particles at different frequencies and HRTs using acoustic standing waves. *Environmental Technology*, *36*, 302–309. https://doi.org/10.1080/09593330.2014.946096

Andrade, E. N. D. C. (1931). Phenomena in a sounding tube. *Nature*, *127*, 438.

Brandt, E. H. (1989). Levitation physics. *Science*, *243*, 349–355. https://doi.org/10.1126/science.243.4889.349

Brandt, E. H. (2001). Acoustic physics—Suspended by sound. *Nature*, *413*, 474–475. https://doi.org/10.1038/35097192

Bruus, H. (2012). Acoustofluidics 7: The acoustic radiation force on small particles. *Lab on a Chip*, *12*, 1014–1021. https://doi.org/10.1039/c2lc21068a

Chen, H., Luo, Z., Jiang, J., Zhou, D., Lu, M., Fang, M., et al. (2015). Effects of simultaneous acoustic and electric fields on removal of fine particles emitted from coal combustion. *Powder Technology*, *281*, 12–19. https://doi.org/10.1016/j.powtec.2015.04.049

Cheng, M., Dong, W., & Qiao, Z. (2016). Experimental study on structured complex acoustic field and its effectiveness of particle manipulation. *Journal of Southeast University (Natural Science Edition)*, *46*, 720–726.

Fan, F., Xu, X., Zhang, S., & Su, M. (2019). Modeling of particle interaction dynamics in standing wave acoustic field. *Aerosol Science and Technology*, *53*, 1204–1216. https://doi.org/10.1080/02786826.2019.1652724

Fleury, R., Sounas, D., & Alu, A. (2015). An invisible acoustic sensor based on parity-time symmetry. *Nature Communications*, *6*, 5905. https://doi.org/10.1038/ncomms6905

Gallego-Juarez, J. A., De Sarabia, E., Rodriguez-Corral, G., Hoffmann, T. L., Galvez-Moraleda, J. C., Rodriguez-Maroto, J. J., et al. (1999). Application of acoustic agglomeration to reduce fine particle emissions from coal combustion plants. *Environmental Science & Technology*, *33*, 3843–3849. https://doi.org/10.1021/es990002n

Gor'Kov, L. (1962). On the forces acting on a small particle in an acoustical field in an ideal fluid. *Soviet Physics Doklady*, *6*, 773–775.

Gubaidullin, D. A., Ossipov, P. P., & Abdyushev, A. A. (2018). Simulation of aerosol distribution in hyperbolic resonator. *Applied Mathematical Modelling*, *62*, 181–193. https://doi.org/10.1016/j.apm.2018.05.028

Guo, J., Chen, Z., Shen, B., Wang, J., & Yang, L. (2020). Numerical study on characteristics of particle deposition efficiency on different walls of 90° square bend. *Powder Technology*, *364*, 572–583. https://doi.org/10.1016/j.powtec.2020.01.059

Havey, P., Jaquay, J. T., Holton, M. M., Hussain, N., & Olenick, S. M. (2018). Persistence of sonic deposition on smoke alarms in forensic fire investigations. *Fire Technology*, *54*, 1631–1654. https://doi.org/10.1007/s10694-018-0761-8

He, M., Luo, Z., Lu, M., Liu, S., & Fang, M. (2019). Effects of acoustic and pulse corona discharge coupling field on agglomeration and removal of coal-fired fine particles. *Aerosol and Air Quality Research*, *19*, 2585–2596. https://doi.org/10.4209/aaqr.2018.08.0306

Hirayama, R., Plasencia, D. M., Masuda, N., & Subramanian, S. (2019). A volumetric display for visual, tactile and audio presentation using acoustic trapping. *Nature*, *575*, 320–323. https://doi.org/10.1038/s41586-019-1739-5

Karpul, D., Tapson, J., Rapson, M., Jongens, A., & Cohen, G. (2010). Limiting factors in acoustic separation of carbon particles in air. *Journal of the Acoustical Society of America*, *127*, 2153–2158.

Kielpinski, D. (2015). Quantum physics—Quantum sound waves stick together. *Nature*, *527*, 45–46.

Kilikevičienė, K., Kačianauskas, R., Kilikevičius, A., Maknickas, A., Matijošius, J., Rimkus, A., et al. (2020). Experimental investigation of acoustic agglomeration of diesel engine exhaust particles using new created acoustic chamber. *Powder Technology*, *360*, 421–429. https://doi.org/10.1016/j.powtec.2019.09.057

Laurell, T., Petersson, F., & Nilsson, A. (2007). Chip integrated strategies for acoustic separation and manipulation of cells and particles. *Chemical Society Reviews*, *36*, 492–506. https://doi.org/10.1039/b601326k

Lee, P. S., Cheng, M. T., & Shaw, D. T. (1982). The influence of hydrodynamic turbulence on acoustic turbulent agglomeration. *Aerosol Science and Technology*, *1*, 47–58. https://doi.org/10.1080/02786828208958578

Liu, J. Z., Wang, J., Zhang, G. X., Zhou, J. H., & Cen, K. F. (2011). Frequency comparative study of coal-fired fly ash acoustic agglomeration. *Journal of Environmental Sciences*, *23*, 1845–1851.

Liu, J. Z., Zhang, G. X., Zhou, J. H., Wang, J., Zhao, W. D., & Cen, K. F. (2009). Experimental study of acoustic agglomeration of coal-fired fly ash particles at low frequencies. *Powder Technology*, *193*, 20–25. https://doi.org/10.1016/j.powtec.2009.02.002

Melde, K., Mark, A. G., Qiu, T., & Fischer, P. (2016). Holograms for acoustics. *Nature*, *537*, 518–522. https://doi.org/10.1038/nature19755

Neild, A. (2016). Acoustics motion controlled by sound. *Nature*, *537*, 493–494. https://doi.org/10.1038/537493a

Pui, D. Y. H., Chen, S., & Zuo, Z. (2014). PM2.5 in China: Measurements, sources, visibility and health effects, and mitigation. *Particuology*, *13*, 1–26. https://doi.org/10.1016/j.partic.2013.11.001

Qiao, Z., Dong, W., Huang, Y., & Naso, V. (2018). Effect of temperature tuning on the aerosol acoustic aggregation process. *Journal of Environmental Sciences*, *67*, 161–170. https://doi.org/10.1016/j.jes.2017.08.021

Qiao, Z., Huang, Y., & Dong, W. (2014). Acoustic resonance characteristics of symmetric cylindrical waveguide with Helmholtz sound source. *Journal of Southeast University (Natural Science Edition)*, *44*, 579–584.

Qiao, Z., Huang, Y., Vincenzo, N., & Dong, W. (2015). Aerosol manipulation by acoustic tunable phase-control at resonant frequency. *Powder Technology*, *281*, 76–82. https://doi.org/10.1016/j.powtec.2015.04.081

Qiao, Z., Liang, S., Pan, X., Bi, X., Zhang, S., Bian, C., et al. (2020). Aerosol aggregation through modulated symmetrically opposing acoustic field in normal 16-sided waveguide coupled with resonators. *Powder Technology*, *364*, 738–745. https://doi.org/10.1016/j.powtec.2020.02.032

Qiao, Z., Huang, Y., Naso, V., & Dong, W. (2017a). Aerosol manipulation through modulated multiple acoustic wavepackets with a pair of resonators. *Powder Technology*, *322*, 24–31. https://doi.org/10.1016/j.powtec.2017.08.062

Qiao, Z., Huang, Y., Naso, V., & Dong, W. (2017b). The advantage of aerosol manipulation by twin types of acoustic resonances. *Journal of Clean Energy Technologies*, *5*, 142–146. https://doi.org/10.18178/jocet.2017.5.2.359

Scales, J. A., & Snieder, R. (1999). What is a wave? *Nature*, *401*, 739–740. https://doi.org/10.1038/44453

Shen, G., Huang, X., He, C., Zhang, S., & An, L. (2018). Experimental study of acoustic agglomeration and fragmentation on coal-fired ash with different particle size distribution. *Powder Technology*, *325*, 145–150. https://doi.org/10.1016/j.powtec.2017.10.037

Shi, Y., Wei, J., Qiu, J., Chu, H., Bai, W., & Wang, G. (2020). Numerical study of acoustic agglomeration process of droplet aerosol using a three-dimensional CFD-DEM coupled model. *Powder Technology*, *362*, 37–53. https://doi.org/10.1016/j.powtec.2019.12.017

Sirtori, C., Barbieri, S., & Colombelli, R. (2013). Wave engineering with THz quantum cascade lasers. *Nature Photonics*, *7*, 691–701. https://doi.org/10.1038/NPHOTON.2013.208

Strecker, K. E., Partridge, G. B., Truscott, A. G., & Hulet, R. G. (2002). Formation and propagation of matter-wave soliton trains. *Nature*, *417*, 150–153. https://doi.org/10.1038/nature747

Sun, Z., Yang, L., Wu, H., & Wu, X. (2020). Agglomeration and removal characteristics of fine particles from coal combustion under different turbulent flow fields. *Journal of Environmental Sciences*, *89*, 113–124. https://doi.org/10.1016/j.jes.2019.10.004

Vainshtein, P., & Shapiro, M. (2011). Trap of a submicron particle in a quadrupole acoustic chamber. *Particulate Science and Technology*, *29*, 450–465. https://doi.org/10.1080/02726351.2010.510167

Wang, B., Li, S., Dong, S., Xin, R., Jin, R., Zhang, Y., et al. (2018). A new fine particle removal technology: cloud-air-purifying. *Industrial & Engineering Chemistry Research*, *57*, 11815–11825. https://doi.org/10.1021/acs.iecr.8b03034

Weiser, M., Apfel, R. E., & Neppiras, E. A. (1984). Interparticle forces on red-cells in a standing wave field. *Acustica*, *56*, 114–119.

Xu, X., Zhang, Q., Hao, M., Hu, Y., Lin, Z., Peng, L., et al. (2019). Double-negative-index ceramic aerogels for thermal superinsulation. *Science*, *363*, 723. https://doi.org/10.1126/science.aav7304

Yan, J., Chen, L., & Li, Z. (2016). Removal of fine particles from coal combustion in the combined effect of acoustic agglomeration and seed droplets with wetting agent. *Fuel*, *165*, 316–323. https://doi.org/10.1016/j.fuel.2015.10.077

Yan, J., Lin, Q., Zhao, S., & Chen, L. (2018). Effect of seed nuclei combined with acoustic field on fine particles removal. *Powder Technology*, *340*, 8–16. https://doi.org/10.1016/j.powtec.2018.09.020

Yuen, W. T., Fu, S. C., & Chao, C. Y. H. (2017). The effect of aerosol size distribution and concentration on the removal efficiency of an acoustic aerosol removal system. *Journal of Aerosol Science*, *104*, 79–89. https://doi.org/10.1016/j.jaerosci.2016.11.014

Zhang, G., Ma, Z., Shen, J., Zhang, K., Wang, J., & Chi, Z. (2020). Experimental study on eliminating fire smokes using acoustic agglomeration technology. *Journal of*

Hazardous Materials, *382*, Article 121089 https://doi.org/10.1016/j.jhazmat.2019.121089
Zhang, G., Zhou, T., Zhang, L., Wang, J., Chi, Z., & Hu, E. (2018). Improving acoustic agglomeration efficiency of coal-fired fly-ash particles by addition of liquid binders. *Chemical Engineering Journal*, *334*, 891–899. https://doi.org/10.1016/j.cej.2017.10.126
Zheng, J., Li, Y., Wan, Z., Hong, W., & Wang, L. (2019). Modification of the agglomeration kernel and simulation of the flow pattern in acoustic field with fine particles. *Powder Technology*, *356*, 930–940. https://doi.org/10.1016/j.powtec.2019.09.022
Zhou, D., Luo, Z., Fang, M., Lu, M., Jiang, J., Chen, H., et al. (2017). Numerical calculation of particle movement in sound wave fields and experimental verification through high-speed photography. *Applied Energy*, *185*, 2245–2250. https://doi.org/10.1016/j.apenergy.2016.02.006
Zhou, D., Luo, Z., Jiang, J., Chen, H., Lu, M., & Fang, M. (2016). Experimental study on improving the efficiency of dust removers by using acoustic agglomeration as pretreatment. *Powder Technology*, *289*, 52–59. https://doi.org/10.1016/j.powtec.2015.11.009